nature communications

Article

https://doi.org/10.1038/s41467-024-52073-3

Enhanced generation of internal tides under global warming

Received: 23 April 2024

Accepted: 26 August 2024

Published online: 03 September 2024

Check for updates

Zhibin Yang[1], Zhao Jing[1,2] ✉, Xiaoming Zhai[3], Clément Vic[4], Hui Sun[2], Casimir de Lavergne[5] & Man Yuan[2]

A primary driver of deep-ocean mixing is breaking of internal tides generated via interactions of barotropic tides with topography. It is important to understand how the energy conversion from barotropic to internal tides responds to global warming. Here we address this question by applying a linear model of internal tide generation to coupled global climate model simulations under a high carbon emission scenario. The energy conversion to high-mode internal tides is projected to rise by about 8% by the end of the 21st century, whereas the energy conversion to low-mode internal tides remains nearly unchanged. The intensified near-bottom stratification under global warming increases energy conversion into both low and high-mode internal tides. In contrast, the intensified depth-averaged stratification reduces the modal horizontal wavenumber of internal tides, leading to increased (decreased) energy conversion into high (low)- mode internal tides. Our findings imply stronger mixing over rough topography under global warming, which should be properly parameterized in climate models for more accurate projections of future climate changes.

The meridional overturning circulation (MOC), connecting the deep ocean with the atmosphere, plays a central role in the climate system by transporting heat, fresh water and carbon across the globe. Model studies have consistently shown that the structure and strength of the MOC depend sensitively on the deep-ocean turbulent diapycnal mixing[1–6] (hereafter referred to as mixing). The geographical distribution of mixing in the ocean is highly inhomogeneous[7–11]. Enhanced mixing is typically observed over rough topography, associated with the local breaking of internal tides (also known as baroclinic tides) generated by interactions of barotropic tides with rough topography[12–15]. The global energy conversion from barotropic tides to baroclinic tides is estimated to be approximately 1 TW[16], a large proportion of the estimated power needed to maintain the MOC[17].

Vertical structures of internal tides are usually described by the eigenmodes related to ocean stratification[18]. The modal partition of tidal energy conversion shapes the geographical pattern of mixing and is a cornerstone of tidal mixing parameterization[3,19,20]. On the one hand, low-mode (e.g., mode 1–3) internal tides, having small vertical shear and large horizontal group velocity, can radiate over a long distance away from their generation sites before dissipation, contributing to the background mixing over the global ocean[21]. On the other hand, high-mode (≥4) internal tides tend to dissipate locally due to their large vertical shear and slow horizontal group velocity, resulting in hotspots for mixing over rough topography[12,22].

In most of the state-of-the-art coupled global climate models (CGCMs)[23–28], the tidal energy conversion and its modal partition are simply assumed to be constant over time. However, the increased emission of greenhouse gases and subsequent ignition of a global warming has enhanced the stratification, especially, in the upper ocean[29,30]. There is a prevailing thought that the enhanced

[1]Laoshan Laboratory, Qingdao, China. [2]Frontier Science Center for Deep Ocean Multispheres and Earth System (FDOMES) and Physical Oceanography Laboratory, Ocean University of China, Qingdao, China. [3]Centre for Ocean and Atmospheric Sciences, School of Environmental Sciences, University of East Anglia, Norwich, UK. [4]University of Brest, CNRS, Ifremer, IRD, Laboratoire d'Océanographie Physique et Spatiale (LOPS), IUEM, Plouzané, France. [5]LOCEAN Laboratory, Sorbonne Université/IRD/CNRS/MNHN, Paris, France. ✉e-mail: jingzhao@ouc.edu.cn

stratification would weaken ocean mixing by suppressing the instability processes responsible for turbulence generation[31,32]. However, this thought overlooks the important effects of stratification on the energy conversion from barotropic to baroclinic tides for different vertical modes[33]. There have been some regional studies showing that the enhanced stratification could result in locally enhanced or reduced tidal energy conversion[34–36]. Yet it remains unclear how the tidal energy conversion and its modal partition respond to global warming on a global scale. Such knowledge is necessary for a more consistent projection of future climate change, particularly in view of the crucial role of tidal mixing in maintaining the MOC[1–6].

In this study, we investigate the response of tidal energy conversion and its modal partition to the enhanced stratification under global warming using a linear model of internal tide generation[12] and simulations from an ensemble of global coupled climate models (CGCMs) in the Coupled Model Intercomparison Project phase 6 (CMIP6) under a high carbon emission scenario[24] ('CMIP6 CGCMs' in Methods). We show that the changes in low-mode tidal energy conversion are spatially inhomogeneous, resulting in a nearly negligible increase (0.9 ± 0.2%) of the globally integrated conversion rate. In contrast, there is a universal increase of the high-mode tidal energy conversion, with its global integral projected to rise by 7.8 ± 0.7% by the end of this century, compared to its present level. This enhanced high-mode tidal energy conversion implies stronger deep-ocean tidal mixing over rough topography and needs to be properly parameterized in CGCMs for a more reliable projection of future climate changes.

Results

Projected future changes of ocean stratification under global warming

The tidal energy conversion and its modal partition depend on both the near-bottom (N_b) and depth-averaged buoyancy frequency ($\bar{N}$) ('Computation of tidal energy conversion' in Methods). On the one hand, the tidal energy conversion for any n-th mode E^n becomes larger with the increasing N_b. In particular, the dependence of E^n on N_b is the same among individual modes and almost linear provided that N_b is much larger than the tidal frequencies, which holds over many parts of the global ocean (Fig. 1a). On the other hand, the effect of $\bar{N}$ on E^n is more complicated, depending on the spectral density of tidal energy conversion in the horizontal wavenumber space ('Computation of tidal energy conversion' in Methods). A larger (smaller) $\bar{N}$ reduces (increases) the modal horizontal wavenumber K^n of internal tides for the n-th mode. For a negative slope of the spectral density of tidal energy conversion, a reduced K^n results in an increase of E^n. The opposite is true when the slope is positive.

The climatological mean (1995–2004) N_b in the observations[37] ('Observational dataset' in Methods) varies by an order of magnitude over the global ocean (Fig. 1a). The geographical distribution of N_b is tightly related to the sea floor depth, with larger values of N_b generally occurring in shallower regions with rougher topography (Supplementary Fig. 1; 'Definition of sea floor roughness' in Methods). There is also prominent geographical variability of climatological mean $\bar{N}$ (Fig. 1b). In contrast to N_b, variability of $\bar{N}$ is primarily

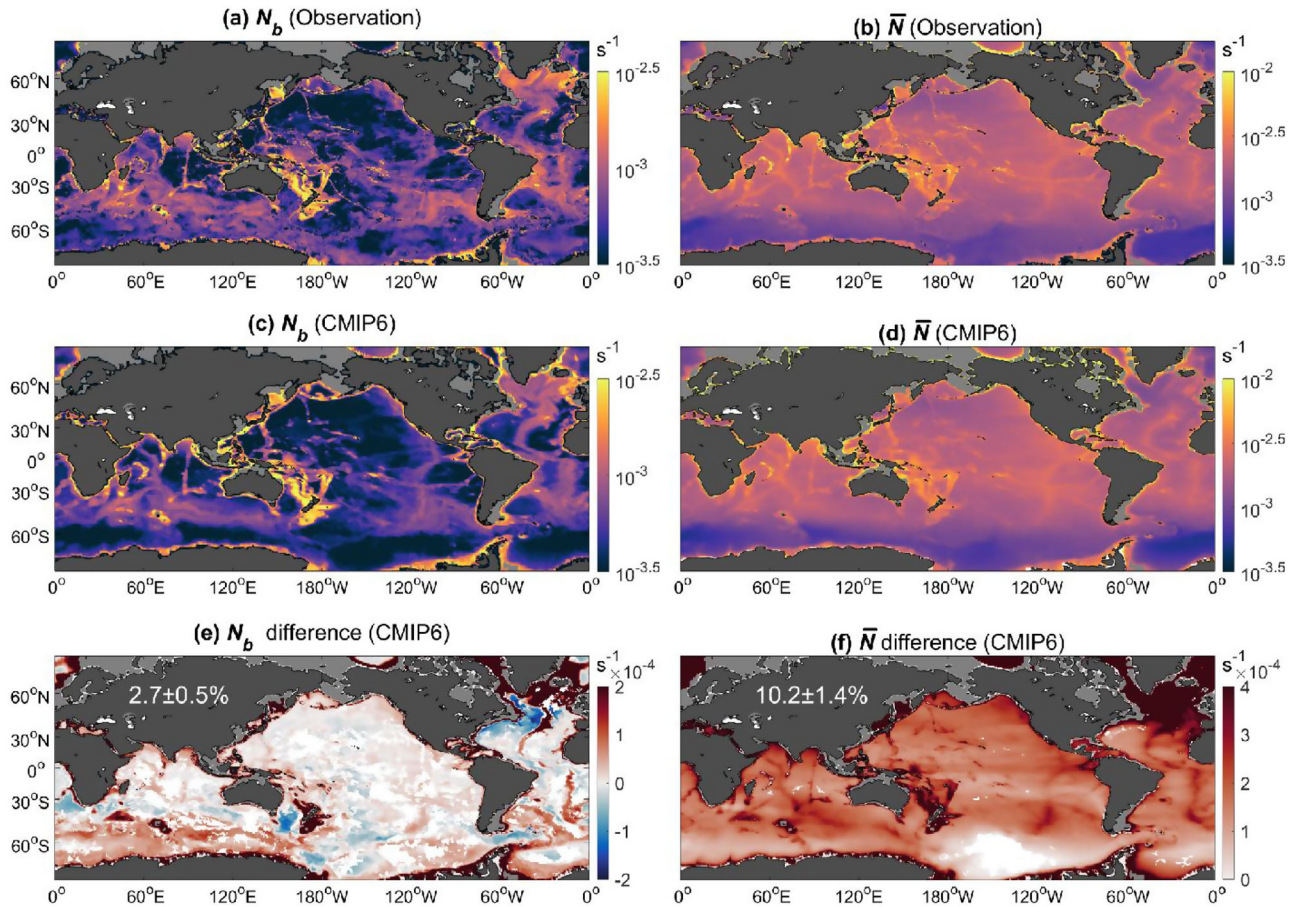

Fig. 1 | Response of near-bottom buoyancy frequency and depth-averaged buoyancy frequency to global warming. a–d Geographical distribution of time-mean (1995–2004) near-bottom buoyancy frequency N_b and depth-averaged buoyancy frequency $\overline{N}$ in the observation (**a**, **b**) and CMIP6 coupled global climate models (CGCMs) ensemble mean (**c**, **d**). **e**, **f** Projected changes (2091–2100 minus 1995–2004) of N_b and $\overline{N}$ in the CMIP6 CGCM ensemble mean. Changes insignificant at a 95% confidence level are filled in white. Numbers in white represent the globally averaged changes in percentage as well as their 95% confidence interval. Areas shallower than 500 m are filled in gray and discarded in the analysis.

controlled by the latitude, with large and small values residing in the tropical and polar oceans, respectively. Nevertheless, imprint of sea floor depth on the geographical distribution of $\bar{N}$ is still noticeable in some regions (e.g., the mid-ocean ridges). The magnitudes and geographical distributions of climatological mean N_b and $\bar{N}$ are well reproduced by the CMIP6 CGCM ensemble mean (Fig. 1c, d), lending support to these CGCMs' fidelity in representing large-scale ocean stratification.

The value of $\bar{N}$ in the CMIP6 CGCM ensemble mean exhibits a universal increase over the global ocean in response to global warming. Its global average during 2091–2100 is projected to be 10.2 ± 1.4% larger than that during 1995–2004 (Fig. 1f). In contrast, the response of N_b to global warming is weaker and heterogeneous (Fig. 1e), with patches of positive and negative trends. The globally averaged N_b is projected to increase only by 2.7 ± 0.5% from 1995–2004 to 2091–2100. It thus suggests that even under a high carbon emission scenario, ocean warming is mainly confined to the upper ocean by the end of 21st century and has a stronger impact on the global mean $\bar{N}$ than N_b.

Projected future changes of tidal energy conversion and its modal partition under global warming

The tidal energy conversion into the first 50 modes E^{1-50} as well as its partition into low modes (E^{1-3}) and high modes (E^{4-50}) is estimated from the linear theory ('Computation of tidal energy conversion' in Methods; Supplementary Fig. 2). Here the computation is limited to the first 50 modes, as the resolution (15-arc second) of the bathymetric dataset ('Observational dataset' in Methods) does not allow to resolve higher modes[38]. Nevertheless, these unresolved higher modes have a much smaller energy conversion than the resolved ones[39]. The globally integrated climatological mean E^{1-50} is 864 GW. Most of this energy conversion occurs over the rough topography such as steep ridges and seamounts (Fig. 2a). The climatological mean E^{1-3} and E^{4-50} have similar geographical distributions to that of E^{1-50} (Fig. 2a–c). The globally integrated climatological mean E^{1-3} and E^{4-50} are 568 GW and 296 GW, respectively.

Under global warming, E^{1-50} is increased over most parts of the global ocean (Fig. 2d). The increase of E^{1-50} is most evident over the rough topography where its climatological mean value is large. The increase of E^{1-50} is primarily attributed to E^{4-50}. The globally integrated E^{1-50} increases by 28 ± 3.5 GW from 1995–2004 to 2091–2100, with E^{4-50} contributing to 23 ± 2.2 GW of this increase. In contrast, the change of E^{1-3} under global warming has both positive and negative values. The globally integrated E^{1-3} increases only by 5 ± 1.3 GW (Fig. 2e). Therefore, the effect of global warming on E^{1-50} is dominated by E^{4-50} whose global integral increases by about 8% by the end of 21st century, compared to its historical (1995–2004) level (Fig. 2c). We remark that such trends of tidal energy conversion and its modal partition do not only hold for the CMIP6 CGCM ensemble mean but also for most of the individual CGCM members (Fig. 3).

Both changes of N_b and $\bar{N}$ can affect the response of tidal energy conversion and its modal partition to global warming. To separate their effects, the change of E^n under global warming is recomputed by either fixing N_b or $\bar{N}$ at its historical (1995–2004) mean value. The changes of N_b and $\bar{N}$ play a comparable role in the increase of E^{1-50} under global warming (Fig. 4a, d), contributing to 16 ± 5.1 GW and 12 ± 3.8 GW, respectively. However, they have distinct effects on the modal partition of tidal energy conversion (Fig. 4b, c, e, f). On the one hand, the enhanced N_b under global warming increases the global integrals of E^{1-3} and E^{4-50} by a similar fraction (2.1 ± 0.5% *vs.* 1.4 ± 0.7%). This is consistent with the nearly linear dependence of E^n on N_b ('Computation of tidal energy conversion' in Methods). On the other hand, the enhanced $\bar{N}$ under global warming decreases the globally integrated E^{1-3} by 6 ± 0.6 GW, whereas it increases the globally integrated E^{4-50} by 18 ± 3.9 GW. As the effects of enhanced N_b and $\bar{N}$ on E^{1-3} (E^{4-50}) counteract (reinforce) each other, this explains the much larger increase of E^{4-50} than E^{1-3} under global warming.

The opposite effects of enhanced $\bar{N}$ on E^{1-3} and E^{4-50} under global warming can be understood based on the reduced K^n in response to the enhanced $\bar{N}$. This is demonstrated by using the M_2 internal tides as a representative example (Supplementary Fig. 3). The energy conversion into the M_2 internal tides is the main contributor to the total tidal energy conversion[40] and its change under global warming (Fig. 2 and Supplementary Fig. 4). Specifically, the geographical distribution of time-mean $E^{1-50}_{M_2}$ during 1995–2004 is highly consistent with that of

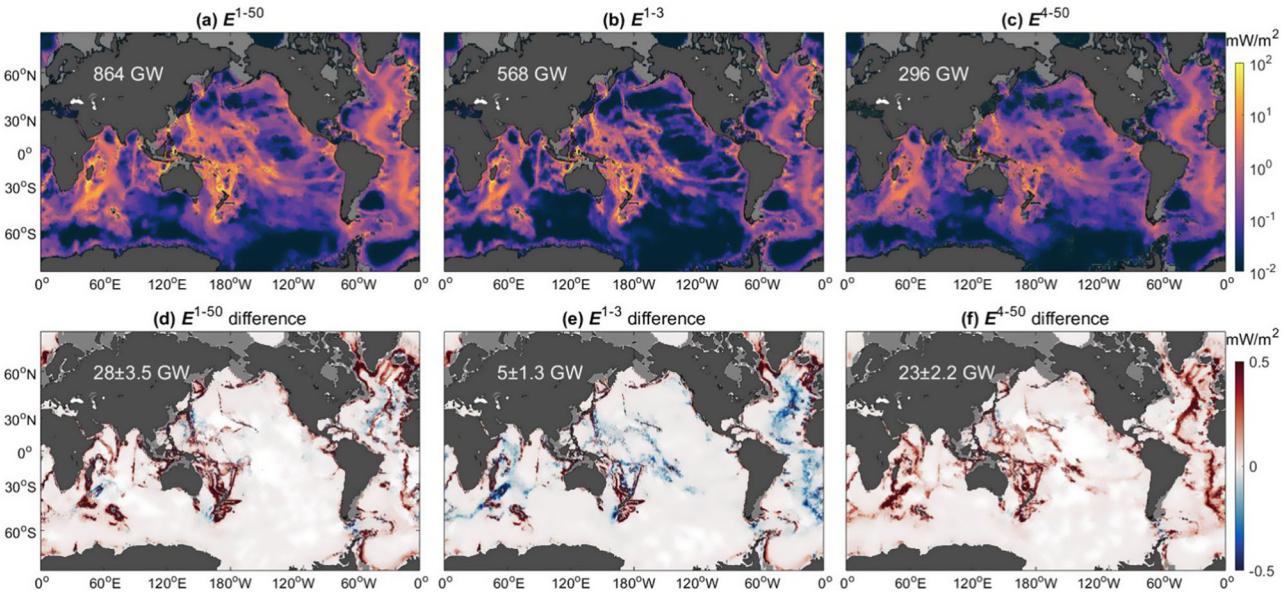

Fig. 2 | Response of tidal energy conversion and its modal partition to global warming. a–c, Geographical distribution of time-mean (1995–2004) of total tidal energy conversion E^{1-50} (**a**), and its partition into low modes E^{1-3} (**b**) and high modes E^{4-50} (**c**). **d–f** Same as **a–c**, but for the projected changes (2091–2100 minus 1995–2004) under global warming. Changes insignificant at a 95% confidence level are filled in white. Numbers in white represent the globally integrated values as well as their 95% confidence interval.

https://doi.org/10.1038/s41467-024-52073-3

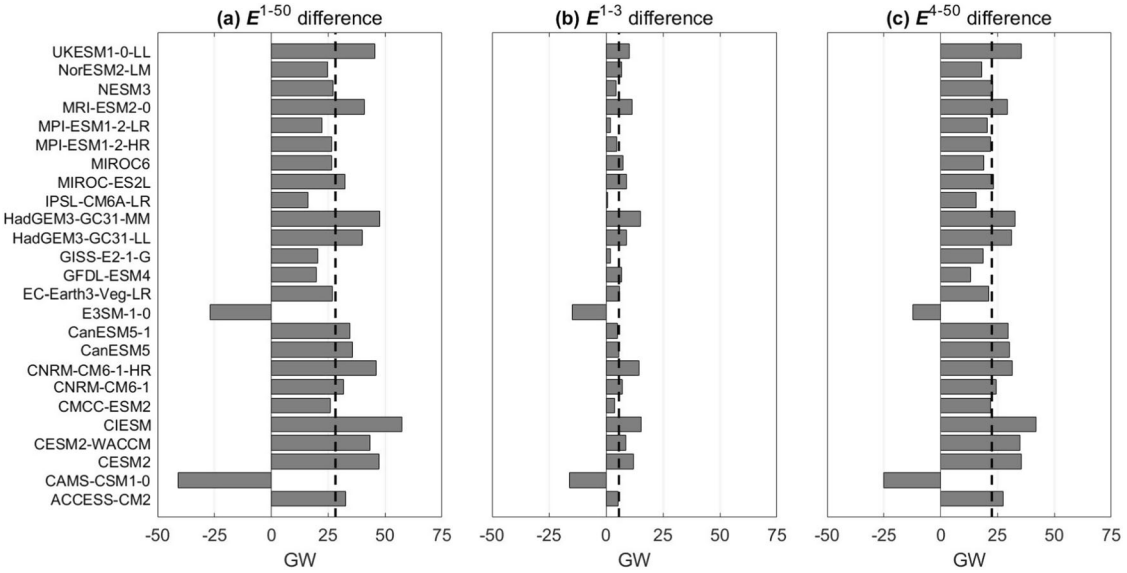

Fig. 3 | Projected changes of globally integrated tidal energy conversion for individual CMIP6 coupled global climate models (CGCMs) members. Changes (2091–2100 minus 1995–2004) of total tidal energy conversion $E^{1\text{-}50}$ (**a**), and its partition into low modes $E^{1\text{-}3}$ (**b**) and high modes $E^{4\text{-}50}$(**c**). Black dashed lines represent their ensemble mean results.

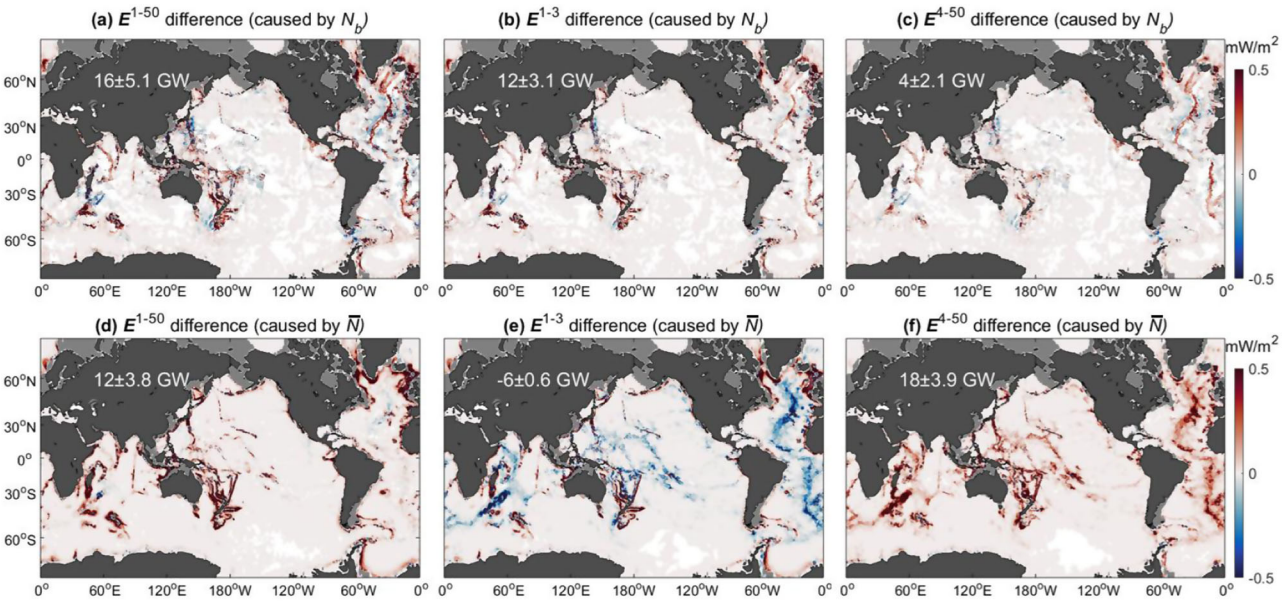

Fig. 4 | Effects of near-bottom buoyancy frequency and depth-averaged buoyancy frequency changes on the tidal energy conversion change under global warming. a–c Geographical distribution of the projected changes (2091–2100 minus 1995–2004) of total tidal energy conversion $E^{1\text{-}50}$ (**a**, **d**), and its partition into low modes $E^{1\text{-}3}$ (b,e) and high modes $E^{4\text{-}50}$ (**c**, **f**), caused by the changes of near-bottom buoyancy frequency N_b (**a**–**c**) and depth-averaged buoyancy frequency $\overline{N}$ (**d**–**f**), respectively. Changes insignificant at a 95% confidence level are filled in white. Numbers in white represent the globally integrated values as well as their 95% confidence interval.

$E^{1\text{-}50}$ with a correlation coefficient of 0.97 (Fig. 2a and Supplementary Fig. 4a). Under global warming, $E^{1-50}_{M_2}$ shows an increase over the major part of the global ocean with its globally integrated increase dominated by that of $E^{4-50}_{M_2}$ (Supplementary Fig. 4).

The spectral density $\Psi_{M_2}(K)$ of M_2 tidal energy conversion in the horizontal wavenumber space, tightly related to the topographic spectrum, shows distinct features between the regions with enhanced and reduced $E^{1-3}_{M_2}$ under global warming. In regions where $E^{1-3}_{M_2}$ is enhanced, the topographic spectrum rolls off rapidly (Supplementary Fig. 5a) and $\Psi_{M_2}(K)$ decreases monotonically as K increases. (Fig. 5a). As $K^n_{M_2}$ is reduced in response to the enhanced $\overline{N}$ (Supplementary Fig. 3), this leads to larger $\Psi_{M_2}(K^n_{M_2})$ for any n under global warming, increasing both $E^{1-3}_{M_2}$ and $E^{4-50}_{M_2}$. In regions with reduced $E^{1-3}_{M_2}$, the topographic spectrum becomes relatively flat (Supplementary Fig. 5b) and $\Psi_{M_2}(K)$ peaks around $K^3_{M_2}$ and attenuates towards both sides (Fig. 5b). Consequently, the reduced $K^n_{M_2}$ under global warming leads to an increase (decrease) of $E^{4-50}_{M_2}$ ($E^{1-3}_{M_2}$) there. In summary, the reduced $K^n_{M_2}$ always increases $E^{4-50}_{M_2}$, whereas its effect on $E^{1-3}_{M_2}$ is region-dependent and relies on the shape of topography spectrum. This explains why the enhanced $\overline{N}$ under global warming leads to an increase in $E^{4\text{-}50}$ but an overall decrease in $E^{1\text{-}3}$.

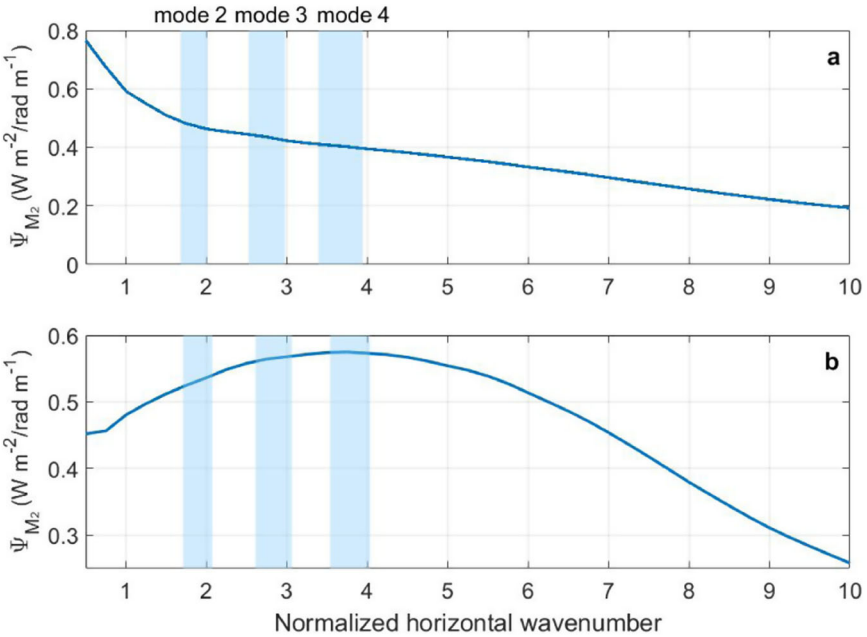

Fig. 5 | Effects of modal horizontal wavenumber change on the energy conversion to M_2 internal tides. Spectral density of M_2 tidal energy conversion (Ψ_{M_2}) as a function of horizontal wavenumber normalized by the mode-1 horizontal wavenumber of M_2 internal tides $K^1_{M_2}$ during 1995–2004, averaged over the regions with the increased **(a)** and decreased **(b)** $E^{1-3}_{M_2}$ under global warming. The color shadings denote the interquartile ranges of $K^2_{M_2}/K^1_{M_2}$, $K^3_{M_2}/K^1_{M_2}$ and $K^4_{M_2}/K^1_{M_2}$.

Discussion

In this study, the response of tidal energy conversion and its modal partition to global warming is evaluated by applying a linear model of internal tide generation to an ensemble of CGCM simulations under a high carbon emission scenario. Although E^{1-3} remains nearly unchanged, E^{4-50} is projected to rise by about 8% by the end of the 21st century, compared to its historical (1995–2004) level. It should be noted that the enhanced E^{4-50} and its dominant contribution to the increase of E^{1-50} is a qualitatively robust response to global warming, regardless of the time periods (Supplementary Fig. 6) and carbon emission scenarios (Supplementary Fig. 7). In particular, E^{4-50} is projected to rise by about 5% by the end of the 21st century under a medium carbon emission scenario[41] that may be accepted by most countries pursuing sustainable growth.

Both the intensified near-bottom stratification and depth-averaged stratification play an important role in the changes of tidal energy conversion under global warming. However, their effects on the modal partition of tidal energy conversion are distinct from each other. The intensified near-bottom stratification increases both E^{1-3} and E^{4-50}, whereas the intensified depth-averaged stratification increases E^{4-50} but reduces E^{1-3}.

Our results suggest that the enhanced stratification under global warming increases energy conversion into high-mode internal tides which largely break near their generation sites and power the deep-ocean mixing locally[7,12]. Such an effect alone would enhance the deep-ocean mixing over the rough topography, leading to "hotter" mixing hotspots in a warming climate. However, the enhanced stratification also acts to suppress mixing as indicated by the Osborn relation[42]. Here we use a tidal mixing parameterization for high-mode internal tides[43] ('Tidal mixing parameterization for high-mode internal tides' in Methods) to explore the relative importance of these two counteracting effects of enhanced stratification on deep-ocean mixing.

Figure 6 shows the parameterized deep-ocean (bottom 1000 m) diapycnal diffusivity κ_ρ resulting from the breaking of high-mode internal tides in the historical period and its future change under global warming. The magnitude of historical κ_ρ varies substantially in space, with mixing hotspots (κ_ρ in the order of O(10^{-3} m^{2}s^{-1})) over rough topography (Fig. 6a). Under global warming, the value of κ_ρ increases over most parts of the global ocean, with the mixing hotspots generally becoming "hotter" (Fig. 6b). It thus suggests that the effect of enhanced stratification on energy conversion into high-mode internal tides plays a dominant role in the response of κ_ρ to global warming. The magnitude of globally averaged κ_ρ during 2091–2100 is projected to increase by 6% compared to its historical level. But locally this value can reach more than 20%.

The increase of κ_ρ caused by enhanced E^{4-50} may have important implications on the MOC and dianeutral upwelling[4,44,45]. Our preliminary analyzes suggest that it could accelerate the lower limb of the Atlantic MOC (AMOC) by about 10% (Supplementary Note 1 and Fig. 8). This change is comparable in magnitude to the projected slowdown (-10%) of the lower limb of the AMOC under a high carbon emission scenario caused by the intrusion of the Antarctic Bottom Water[46]. Furthermore, there is a significant response of the dianeutral upwelling to the enhanced E^{4-50} (Supplementary Note 2 and Fig. 9). The peak of the globally integrated dianeutral upwelling increases by about 10%. In view of the uncertainties in the tidal mixing parameterization[42], the above results should be treated as suggestive rather than definitive. Nevertheless, they suggest important effects of the enhanced E^{4-50} resulting from the future stratification changes on tracer and mass transports in the deep ocean. So far the interactivity of parameterized tidal mixing is either neglected or limited in the state-of-the-art CGCMs[23–28]. Integrating stratification changes into tidal mixing parameterizations is imperative for accurately projecting anthropogenic climate changes in the future.

Methods

Observational dataset

We calculate the historical N using the climatological mean (1995–2004) temperature and salinity fields on a 0.25° × 0.25° grid from the World Ocean Atlas 2018 (WOA18)[37]. There are 102 vertical levels in the ocean with a maximum grid size of 100 m at the 5500 m depth. The two-dimensional topographic spectrum is computed from the updated Shuttle Radar Topography Mission dataset (SRTM15+)[47] with a nominal resolution of 15-arc second.

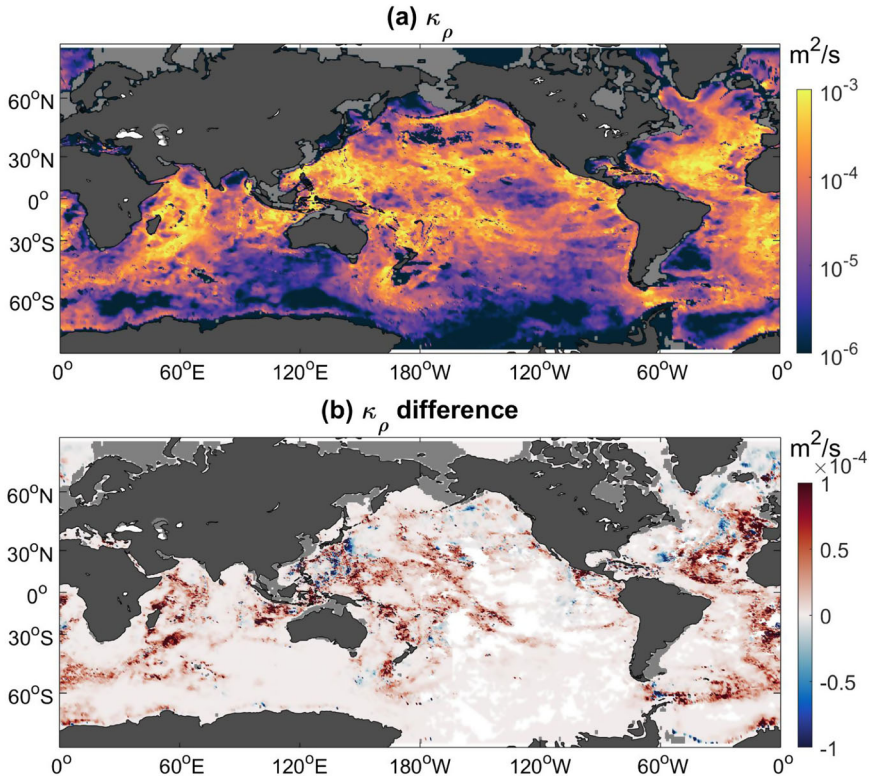

Fig. 6 | Implications of enhanced energy conversion into high-mode internal tides under global warming on the deep-ocean mixing. a Geographical distribution of vertical mean (bottom 1000-m) parameterized diapycnal diffusivity κ_ρ caused by the breaking of high-mode internal tides during 1995–2004. **b** Same as **a** but for the difference between 1995–2004 and 2091–2100. Changes insignificant at a 95% confidence level are filled in white.

CMIP6 CGCMs

In this study, a total of 25 CGCMs from the CMIP6[24] (Supplementary Table 1) are used to estimate the future change of N under the Shared Socioeconomic Pathways (SSP585), denoted as ΔN. The value of ΔN is computed as the simulated time-mean N during 2091–2100 minus that during 1995–2004. To remove the model drift, the counterpart of N change (the last decade minus the decade 96 years ago) in the pre-industrial control (PI-CTRL) simulation is subtracted from ΔN. When computing the tidal energy conversion during 2091–2100, we add ΔN to the observational time-mean N during 1995–2004 to minimize the model bias in the simulated N during the historical period.

Computation of tidal energy conversion

The tidal energy conversion rate is estimated using St. Laurent and Garrett's[12] formulation based on the linear theory proposed by Bell[48,49]:

$$\psi(K,\theta)=\frac{1}{2}\rho_0\frac{[(N_b^2-\omega^2)(\omega^2-f^2)]^{1/2}}{\omega}\times(u_e^2\cos^2\theta+v_e^2\sin^2\theta)K\phi(K,\theta) \quad (1)$$

where $\psi(K,\theta)$ is the spectral density of tidal energy conversion rate in the horizontal wavenumber space, ρ_0 is the reference density, N_b is the near-bottom buoyancy frequency computed as the vertical mean buoyancy frequency within 0–300 m above the sea floor, ω is the tidal frequency, f is the Coriolis frequency, u_e (v_e) is the semi-major (semi-minor) component of the barotropic tidal velocity amplitude retrieved from TPXO8[50], $K=(k^2+l^2)^{1/2}$ is the total horizontal wavenumber with k and l the respective wavenumbers along the semi-major and semi-minor directions, $\theta=\arctan(l/k)$ is the azimuthal angle, and ϕ is the two-dimensional topographic spectrum. The azimuthally averaged spectral density of tidal energy conversion rate can be computed as:

$$\Psi(K)=\frac{1}{2\pi}\int_0^{2\pi}\psi(K,\theta)Kd\theta \quad (2)$$

The vertical modes of internal tides can be determined by solving the Sturm-Liouville problem:

$$\frac{d^2a_n}{dz^2}+c_n^{-2}N^2a_n=0 \quad (3)$$

with homogeneous boundary conditions at the sea floor ($z=-H$) and the sea surface ($z=0$)

$$a_n(0)=a_n(-H)=0 \quad (4)$$

where a_n and c_n are the eigenfunction and eigenspeed for the n-th mode. Once c_n is obtained, the modal horizontal wavenumber can be calculated based on the dispersion relation of internal waves as:

$$K^n=\frac{\sqrt{\omega^2-f^2}}{c_n} \quad (5)$$

Finally, the tidal energy conversion rate into the n-th mode is given by:

$$E^n=\int_{K^n-\delta K/2}^{K^n+\delta K/2}\Psi(K)KdK \quad (6)$$

where $\delta K=K^{n+1}-K^n$.

It should be noted that Eq. (1) derived from the linear theory is only valid for subcritical topography, i.e.,

$$\gamma = \frac{|\nabla h|}{[(\omega^2 - f^2)/(N_b^2 - \omega^2)]^{1/2}} < 1 \quad (7)$$

where $|\nabla h|$ and $[(\omega^2 - f^2)/(N_b^2 - \omega^2)]^{1/2}$ are the slopes of topography and radiated internal tide beams, respectively. The condition for subcritical topography is satisfied over most parts of the ocean, except for shallow regions with strong N_b. For this reason, the computation of Eq. (6) is confined to regions with water depth greater than 500 m. This neglects the downward radiation of internal tides generated in the regions shallower than 500 m to the deep ocean, which is suggested to contribute little to the deep ocean energy budget of internal tides[20]. For areas with supercritical topography ($\gamma > 1$), a correction is implemented on E^n by dividing E^n by γ^2, following Green and Nycander[51] and Vic et al.[38].

The values of E^n are computed for the three main tidal constituents (M_2, S_2, and K_1), which collectively account for about 90% of the total tidal energy conversion[52]. Following de Lavergne et al.[19], we apply a scaling factor to estimate the total energy conversion for the eight principal tidal constituents (M_2, S_2, N_2, K_2, K_1, O_1, P_1, Q_1):

$$E^n = 1.05 \times E^n_{M_2} + 1.09 \times E^n_{S_2} + 1.70 \times E^n_{K_1} \quad (8)$$

Definition of sea floor roughness

The sea floor roughness is calculated as the root-mean-square of topography height in each 0.5 × 0.5° grid cell. Before computing the sea floor roughness, the large-scale topography is removed by subtracting a fitted polynomial plane of topography height[53].

Tidal mixing parameterization for high-mode internal tides

The mixing driven by the local dissipation of high-mode internal tides is parameterized as[38,43]:

$$\kappa_\rho = \frac{\Gamma E^{4-50} F(z)}{\rho_0 N^2} \quad (9)$$

where $\Gamma = 0.2$ is the mixing efficiency[42] and $F(z)$ is the vertical structure function defined as:

$$F(z) = \frac{e^{(z-H)/\eta}}{\eta(1 - e^{-H/\eta})} \quad (10)$$

with a vertical decay scale of $\eta = 500$ m.

Data availability

All data needed to evaluate the conclusions in the paper can be downloaded from the following links: WOA18: https://www.ncei.noaa.gov/products/world-ocean-atlas[37]; SRTM15+: https://figshare.com/articles/online_resource/Tozer_et_al_2019_SRTM15_GMT_Grids/7979780[47]; CMIP6 models: https://esgf-node.llnl.gov/search/cmip6/[24]; TPXO8: https://www.tpxo.net/global[50]. Source data of the main figures is provided with this paper. Source data are provided with this paper.

Code availability

Code link to reproduce the results: https://doi.org/10.5281/zenodo.13346979.

References

1. Samelson, R. M. Large-scale circulation with locally enhanced vertical mixing. *J. Phys. Oceanogr.* **28**, 712–726 (1998).
2. Scott, J. R. & Marotzke, J. The location of diapycnal mixing and the meridional overturning circulation. *J. Phys. Oceanogr.* **32**, 3578–3595 (2002).
3. Simmons, H. L., Jayne, S. R., St. Laurent, L. C. & Weaver, A. J. Tidally driven mixing in a numerical model of the ocean general circulation. *Ocean Model* **6**, 245–263 (2004).
4. Saenko, O. A., Zhai, X., Merryfield, W. J. & Lee, W. G. The combined effect of tidally and eddy-driven diapycnal mixing on the large-scale ocean circulation. *J. Phys. Oceanogr.* **42**, 526–538 (2012).
5. Tatebe, H., Tanaka, Y., Komuro, Y. & Hasumi, H. Impact of deep ocean mixing on the climatic mean state in the Southern Ocean. *Sci. Rep.* **8**, 14479 (2018).
6. Hieronymus, M., Nycander, J., Nilsson, J., Döös, K. & Hallberg, R. Oceanic overturning and heat transport: The role of background diffusivity. *J. Clim.* **32**, 701–716 (2019).
7. Polzin, K., Toole, J., Ledwell, J. & Schmitt, R. Spatial variability of turbulent mixing in the abyssal ocean. *Science* **276**, 93–96 (1997).
8. Kunze, E., Firing, E., Hummon, J. M., Chereskin, T. K. & Thurnherr, A. M. Global abyssal mixing inferred from lowered ADCP shear and CTD strain profiles. *J. Phys. Oceanogr.* **36**, 1553–1576 (2006).
9. Wu, L., Jing, Z., Riser, S. & Visbeck, M. Seasonal and spatial variations of Southern Ocean diapycnal mixing from Argo profiling floats. *Nat. Geosci.* **4**, 363–366 (2011).
10. Whalen, C. B., Talley, L. D. & MacKinnon, J. A. Spatial and temporal variability of global ocean mixing inferred from Argo profiles. *Geophys. Res. Lett.* **39**, 1–6 (2012).
11. Waterhouse, A. F. et al. Global patterns of diapycnal mixing from measurements of the turbulent dissipation rate. *J. Phys. Oceanogr.* **44**, 1854–1872 (2014).
12. St. Laurent, L. & Garrett, C. The role of internal tides in mixing the deep ocean. *J. Phys. Oceanogr.* **32**, 2882–2899 (2002).
13. Klymak, J. M., Pinkel, R. & Rainville, L. Direct breaking of the internal tide near topography: Kaena Ridge, Hawaii. *J. Phys. Oceanogr.* **38**, 380–399 (2008).
14. Tian, J., Yang, Q. & Zhao, W. Enhanced diapycnal mixing in the South China Sea. *J. Phys. Oceanogr.* **39**, 3191–3203 (2009).
15. MacKinnon, J. A. et al. Climate process team on internal wave-driven ocean mixing. *Bull. Am. Meteorol. Soc.* **98**, 2429–2454 (2017).
16. Egbert, G. & Ray, R. Significant dissipation of tidal energy in the deep ocean inferred from satellite altimeter data. *Nature* **405**, 775–778 (2000).
17. Munk, W. & Wunsch, C. Abyssal recipes II: energetics of tidal and wind mixing. *Deep-Sea Res. I* **45**, 1977–2010 (1998).
18. Gill, A. E. & Adrian, E. Atmosphere–Ocean Dynamics Vol. 30 (Academic Press, 1982).
19. de Lavergne, C. et al. Toward global maps of internal tide energy sinks. *Ocean Model* **137**, 52–75 (2019).
20. de Lavergne, C., Vic, C., Madec, G., Roquet, F. & Waterhouse, A. F. A Parameterization of Local and Remote Tidal Mixing. *J. Adv. Model. Earth Syst.* **12** https://doi.org/10.1029/2020MS002065 (2020).
21. Zhao, Z., Alford, M. H., Girton, J. B., Rainville, L. & Simmons, H. L. Global observations of open-ocean mode-1 M2 internal tides. *J. Phys. Oceanogr.* **46**, 1657–1684 (2016).
22. Nikurashin, M. & Legg, S. A mechanism for local dissipation of internal tides generated at rough topography. *J. Phys. Oceanogr.* **41**, 378–395 (2011).
23. Madec, G. et al. NEMO ocean engine. Tech. Rep. (2015).
24. Eyring, V. et al. Overview of the Coupled Model Intercomparison Project Phase 6 (CMIP6) experimental design and organization. *Geosci. Model Dev.* **9**, 1937–1958 (2016).
25. Lin, Y. et al. Community Integrated Earth System Model (CIESM): Description and Evaluation. J. Adv. Model. Earth Syst. 1–29 (2018).
26. Cherchi, A. et al. Global mean climate and main patterns of variability in the CMCC-CM2 coupled model. *J. Adv. Model. Earth Syst.* **11**, 185–209 (2019).

27. Swart, N. C. et al. The canadian earth system model version 5 (CanESM5.0.3). *Geosci. Model Dev.* **12**, 4823–4873 (2019).
28. Bi, D. et al. Configuration and spin-up of ACCESS-CM2, the new generation Australian community climate and earth system simulator coupled model. *J. South. Hemisph. Earth Syst. Sci.* **70**, 225–251 (2020).
29. Li, G. et al. Increasing ocean stratification over the past half-century. *Nat. Clim. Chang.* **10**, 1116–1123 (2020).
30. Sallée, J. B. et al. Summertime increases in upper-ocean stratification and mixed-layer depth. *Nature* **591**, 592–598 (2021).
31. Keith Moore, J. et al. Sustained climate warming drives declining marine biological productivity. *Sci. (80-.).* **359**, 113–1143 (2018).
32. Oschlies, A., Brandt, P., Stramma, L. & Schmidtko, S. Drivers and mechanisms of ocean deoxygenation. *Nat. Geosci.* **11**, 467–473 (2018).
33. Llewellyn Smith, S. G. & Young, W. R. Conversion of the barotropic tide. *J. Phys. Oceanogr.* **32**, 1554–1566 (2002).
34. Decarlo, T. M., Karnauskas, K. B., Davis, K. A. & Wong, G. T. F. Climate modulates internal wave activity in the Northern South China Sea. *Geophys. Res. Lett.* **42**, 831–838 (2015).
35. Yadidya, B. & Rao, A. D. Projected climate variability of internal waves in the Andaman Sea. Commun. Earth Environ. **3**, 2819 (2022).
36. Guo, Z. et al. Variability of the M_2 internal tides in the Luzon Strait under climate change. *Clim. Dyn.* https://doi.org/10.1029/2022JC019281 (2024).
37. Garcia H. E. et al. World Ocean Atlas 2018. NOAA National Centers for Environmental Information. Retrieved from https://www.ncei.noaa.gov/products/world-ocean-atlas (2018).
38. Vic, C. et al. Deep-ocean mixing driven by small-scale internal tides. *Nat. Commun.* **10**, 2099 (2019).
39. Melet, A. et al. Internal tide generation by abyssal hills using analytical theory. *J. Geophys. Res. Ocean.* **118**, 6303–6318 (2013).
40. Egbert, G. D. & Ray, R. D. Semi-diurnal and diurnal tidal dissipation from TOPEX/Poseidon altimetry. *Geophys. Res. Lett.* **30**, 1907 (2003).
41. Meehl, G. A. et al. Climate model intercomparisons: preparing for the next phase. *Eos, Trans. Am. Geophys. Union* **95**, 77–78 (2014).
42. Osborn, T. Estimates of the local rate of vertical diffusion from dissipation measurements. *J. Phys. Oceanogr.* **10**, 8389 (1980).
43. St Laurent, L., Simmons, H. & Jayne, S. Estimating tidally driven mixing in the deep ocean. *Geophys. Res. Lett.* **29**, 21-1–21-4 (2002).
44. Melet, A., Hallberg, R., Legg, S. & Nikurashin, M. Sensitivity of the ocean state to lee wave-driven mixing. *J. Phys. Oceanogr.* **44**, 900–921 (2014).
45. Cimoli, L. et al. Sensitivity of deep ocean mixing to local internal tide breaking and mixing efficiency. *Geophys. Res. Lett.* **46**, 14622–14633 (2019).
46. Heuzé, C., Heywood, K. J., Stevens, D. P. & Ridley, J. K. Changes in global ocean bottom properties and volume transports in CMIP5 models under climate change scenarios. *J. Clim.* **28**, 2917–2944 (2015).
47. Tozer, B. et al. Global bathymetry and topography at 15 Arc Sec: SRTM15+. *Earth Sp. Sci.* **6**, 1847–1864 (2019).
48. Bell, T. Lee waves in stratified flows with simple harmonic time dependence. *J. Fluid Mech.* **67**, 705–722 (1975).
49. Bell, T. Topographically generated internal waves in the open ocean. *J. Geophys. Res.* **80**, 320–327 (1975).
50. Egbert, G. D. & Erofeeva, S. Y. Efficient inverse modeling of barotropic ocean tides. *J. Atmos. Ocean. Technol.* **19**, 183–204 (2002).
51. Green, J. A. M. & Nycander, J. A comparison of tidal conversion parameterizations for tidal models. *J. Phys. Oceanogr.* **43**, 104–119 (2013).
52. Nycander, J. Generation of internal waves in the deep ocean by tides. *J. Geophys. Res.* **110**, C10028 (2005).
53. Jayne, S. R. & St. Laurent, L. C. Parameterizing tidal dissipation over rough topography. *Geophys. Res. Lett.* **28**, 811–814 (2001).

Acknowledgements

This work was supported by the National Natural Science Foundation of China (42325601 and 92358303 to Z.J. and 42306013 to Z.Y.), and Marine S&T Fund of Shandong Province for Laoshan Laboratory (2022QNLM010302 to Z.J.). Computational resources were provided by Laoshan Laboratory.

Author contributions

Z.Y. conducted the analysis under Z.J.'s instruction. Z.J. conceived the project. Z.Y., Z.J. and X.Z. wrote the manuscript, C.d.L. calculated the water mass transformation, and M.Y. performed the POP2 model. Z.Y., Z.J., X.Z., C.V., H.S., C.d.L. and M.Y. were involved in interpreting the results and contributed to improving the manuscript.

Competing interests

The authors declare no competing interests.

Additional information

Supplementary information The online version contains supplementary material available at https://doi.org/10.1038/s41467-024-52073-3.

Correspondence and requests for materials should be addressed to Zhao Jing.

Peer review information *Nature Communications* thanks Peter Brandt and the other, anonymous, reviewer for their contribution to the peer review of this work. A peer review file is available.